

Edge-Selectively Halogenated Graphene Nanoplatelets (XGnPs, X = Cl, Br, or I) Prepared by Ball-Milling and Used as Anode Materials for Lithium-Ion Batteries

Jiantie Xu, In-Yup Jeon, Jeong-Min Seo, Shixue Dou,^{*} Liming Dai,^{*} and Jong-Beom Baek^{*}

It is important to develop lithium-ion batteries (LIBs) with high energy densities for sustainable energy storage.^[1] Great efforts have been devoted to the development of high voltage cathode materials with high specific capacity, long cycle life, and environmental friendliness in order to improve the energy density for LIBs. Among the high voltage cathode materials for LIBs, polyanions XO_4 based compounds (e.g., $LiMPO_4$, M = Fe, Mn, Ni or Co) and lithium metal oxides (e.g., $LiMn_2O_4$, or $LiNi_{0.5}Mn_{1.5}O_2$) have shown high reversible capacities and excellent cycling stability.^[2] Furthermore, these materials doped by halogen element (e.g., fluorine,^[3] chlorine,^[4] bromine^[5] or iodine^[6]) in the oxygen-containing unit (e.g., O^{2-} , PO_4^{3-}) exhibited higher reversible capacity or better cyclability. It is due to the effect of the different electronegativity of halogen atoms ($\chi = 2.66 \sim 3.98$). They have a different ability of electron loss compared to O^{2-} ($\chi = 3.44$). Furthermore, halogen ions X^- have a lower electrostatic repulsion than O^{2-} , facilitating the lithium extraction/insertion,^[7] and thus stabilizing the host structures during the cycling.^[3] To date, the reported research on halogen-containing anode materials is limited,^[3,8] though a large number of halogen incorporated cathode materials have been intensively investigated for high energy LIBs.

Graphene, one of prominent carbon materials, has recently received more and more attention as anode material for LIBs, because of its outstanding capacity, surface area, conductivity, thermal stability, and environmental friendliness. Due to its fascinating properties, graphene as anode for LIBs shows excellent

electrochemical performance.^[9–11] Moreover, many reports have demonstrated that the electrochemical performance of graphene for LIBs was dramatically enhanced by doping with heteroatoms (e.g., N, B, and P).^[12] Recently, our group explored a simple, eco-friendly method by dry ball-milling graphite in the presence of different substances, leading to mass production of various heteroatom-doped graphene nanoplatelets (GnPs).^[13,14] By simply ball-milling graphite with chlorine (Cl_2), bromine (Br_2) or iodine (I_2), for instance, we have successfully prepared a series of edge-selectively halogenated graphene nanoplatelets (XGnPs, X = Cl, Br or I). These edge-functionalized GnPs (EFGnPs) were employed as promising metal-free electrocatalysts for oxygen reduction reaction (ORR) in fuel cells.^[13] The XGnPs displayed excellent electrocatalytic activities with good cycle stability. Compared with other approaches for the production of graphene, including chemical vapor deposition (CVD),^[15] arc-discharge,^[16] Hummer's methods,^[17] and solvothermal synthesis,^[18] this simple, eco-friendly ball-milling method is a low-cost and scalable approach for the production of XGnPs as anode materials to meet the ever-increasing demand of LIBs for our near-term needs, for example in a wide range of electric vehicles.

Here, we report the first study on the use of edge-selectively halogenated GnPs (XGnPs, X = Cl, Br, or I) prepared by the ball-milling method as anode materials for LIBs. For comparison, edge-hydrogenated GnP (HGnP) was also prepared by ball-milling graphite in the presence of hydrogen.^[19] This method employed the repulsive interaction of edge-halogenated groups as the driving force to gradually exfoliate the graphite into XGnPs during the ball-milling process, and thus allowed for a low-cost and large-scale production of XGnPs. It was found that IGnP electrode delivered an initial charge capacity of 562.8 mAh g^{-1} at 0.5 C in the voltage range of 0.02 – 3.0 V, which was higher than the reference HGnP with 511.3 mAh g^{-1} . Furthermore, after 500 cycles, the IGnP electrode was still able to deliver a higher charge capacity of 458.0 mAh g^{-1} with a higher initial charge capacity retention of 81.4% than the HGnP with 208.5 mAh g^{-1} and 40.8%, respectively. After 500 cycles and 1 month storage at ambient condition (25 °C), the IGnP cell still maintained a reversible capacity of 464.1 mAh g^{-1} at the end of additional 100 cycles, indicating a remarkably high stability. Such excellent electrochemical performance of the IGnP as anode for LIBs is attributable to the high electronegativity of I ($\chi = 2.66$ higher than $\chi = 2.55$ for carbon), high surface area of IGnP ($736.8 \text{ m}^2 \text{ g}^{-1}$), as well as the improved lithium-ion insertion/extraction at the edges ($d_I > d_H$) between graphitic layers,^[13] which should lead to

J. Xu,^[†] Prof. S. Dou
Institute for Superconducting
and Electronic Materials
University of Wollongong
Wollongong, NSW 2522, Australia
E-mail: dou@uow.edu.au



J. Xu, Prof. L. Dai
Department of Macromolecular Science and Engineering
Case Western Reserve University
Cleveland, OH 44106, USA
E-mail: liming.dai@case.edu

Dr. I.-Y. Jeon,^[†] J.-M. Seo, Prof. J.-B. Baek
School of Energy and Chemical Engineering/Low-Dimensional
Carbon Materials Center
Ulsan National Institute of Science and Technology (UNIST)
100 Banyeon, Ulsan 689-897, South Korea
E-mail: jbbaek@unist.ac.kr

^[†]These authors contributed equally to this work.

DOI: 10.1002/adma.201402987

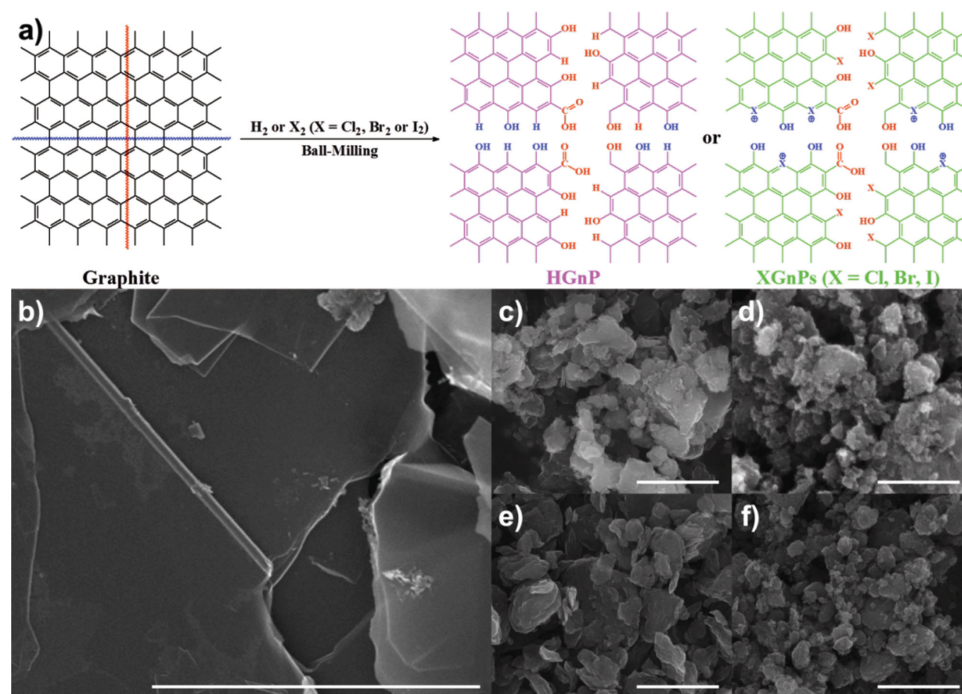


Figure 1. (a) A schematic representation for mechanochemical functionalization at the broken edges of graphene nanoplatelets (GnPs) in the presence of hydrogen (H_2), chlorine (Cl_2), bromine (Br_2) or iodine (I_2) to produce HGnP, ClGnP, BrGnP or IGnP. SEM images: (b) the pristine graphite (100 mesh, <math>< 150 \mu m</math>); (c) HGnP; (d) ClGnP; (e) BrGnP; (f) IGnP. The scale bars are 1 μm . Corresponding element mappings are presented in Figure S1. The average grain size of HGnP and XGnPs ($X = Cl, Br \text{ or } I$) is less than 1 μm .

enhanced lithium-ion transportation through the electrolyte and electrode during cycling.

Figure 1a describes a schematic representation of mechanochemically driven edge-selective functionalization of graphene nanoplatelets (EFGnPs) in the presence of hydrogen (H_2), chlorine (Cl_2), bromine (Br_2) and iodine (I_2) to produce HGnP, ClGnP, BrGnP and IGnP, respectively. Scanning electron microscope (SEM) images show that ball-milling graphite (Figure 1b) reduced the grain size of HGnP (Figure 1c) and XGnPs (Figures 1d–1f). Typical grain sizes of HGnP and XGnPs after ball-milling are less than 1 μm (Figures 1c–1f), while the graphite starting material was up to 150 μm . The dramatic size reduction implies that unzipping of graphitic sp^2 C–C bonds generates active carbon species, which spontaneously react with hydrogen (H_2), chlorine (Cl_2), bromine (Br_2) or iodine (I_2) to produce HGnP, ClGnP, BrGnP or IGnP. The formation of C–H, C–Cl, C–Br or C–I bonds of the resultant HGnP and XGnPs ($X = Cl, Br \text{ or } I$) is confirmed by elemental analysis (EA, Table S1), energy dispersive X-ray (EDX) spectroscopy (Figure 2a and Table S1) with element mapping (Figure S1) and X-ray photoelectron spectroscopy (XPS, Figure 2b). Moreover, high-resolution STEM images (Figures S2–S5) with selected area electron diffraction (SAED) patterns of bulk XGnP powders show flake-like morphology with structural distortions at the edges. The EDX (Figures S2c, S3d, S4d and S5d) and elemental mapping (Figures S2f, S2g, S3g–S2i, S4g–S4i and S5g–S5i) indicate that halogen, carbon and oxygen are uniformly distributed throughout the samples. More detailed structures from the HAADF STEM images (also known as Z-contrast due to the Z-dependence) clearly show the presence of halogen

heteroatoms (bright dots) located along the edges of XGnPs ($X = Cl, Br \text{ or } I$) (Figures S2d, S3e, S4e and S5e).

Detailed element chemical compositions of XGnPs ($X = Cl, Br \text{ or } I$) were analyzed by XPS survey spectra (Figure 2b). Along with the C 1s and O 1s main peaks, the XPS spectra show the characteristic peaks of each sample such as Cl 2p for ClGnP, Br 3s, Br 3p and Br 3s for BrGnP and I 3d, I 4d for IGnP. In addition, element contents of halogen were calculated to be 3.37 at.% of Cl for ClGnP, 2.99 at.% of Br for BrGnP and 1.06 at.% of I for IGnP (Table S1). Chemical bond nature was further studied by using high-resolution XPS spectra of Cl 2p (Figure S6a), Br 3d (Figure S6b) and I 3d (Figure S6c). Each peak has been deconvoluted into various sub-peaks. For example, Cl 2p peak was curve-fitted into Cl $2p_{1/2}$ and Cl $2p_{3/2}$, which signified covalent bonding of Cl with carbon (C–Cl). However, Br 3d and I 3d peaks splitted into the corresponding binding energies for the covalent (C–Br and C–I) and ionic bonds (C–Br $^+$ –C and C–I $^+$ –C). Since the atomic sizes of Br (Row 4) and I (Row 5) are bigger than Cl (Row 3), BrGnP and IGnP can form C–Br $^+$ –C and C–I $^+$ –C bonds in addition to C–Br and C–I bonds (Figures S6b and S6c), respectively. Although the intensities of ionic bonds in BrGnP and IGnP are smaller than those of covalent bonds, the presence of ionic nature may lead to a high electrochemical activity.

Raman spectra were used to reveal the structural difference between HGnP and XGnPs ($X = Cl, Br \text{ or } I$). As can be seen in Figure 2c, all XGnPs show sharp G and D peaks at around 1585 and 1344 cm^{-1} , respectively, with a relatively weaker G band in respect to D band, and thus the peak intensity (I_D/I_G) ratios are in the range of 1.46–1.72. On the other hand, HGnP has a broader and stronger G band than the D peak, and hence

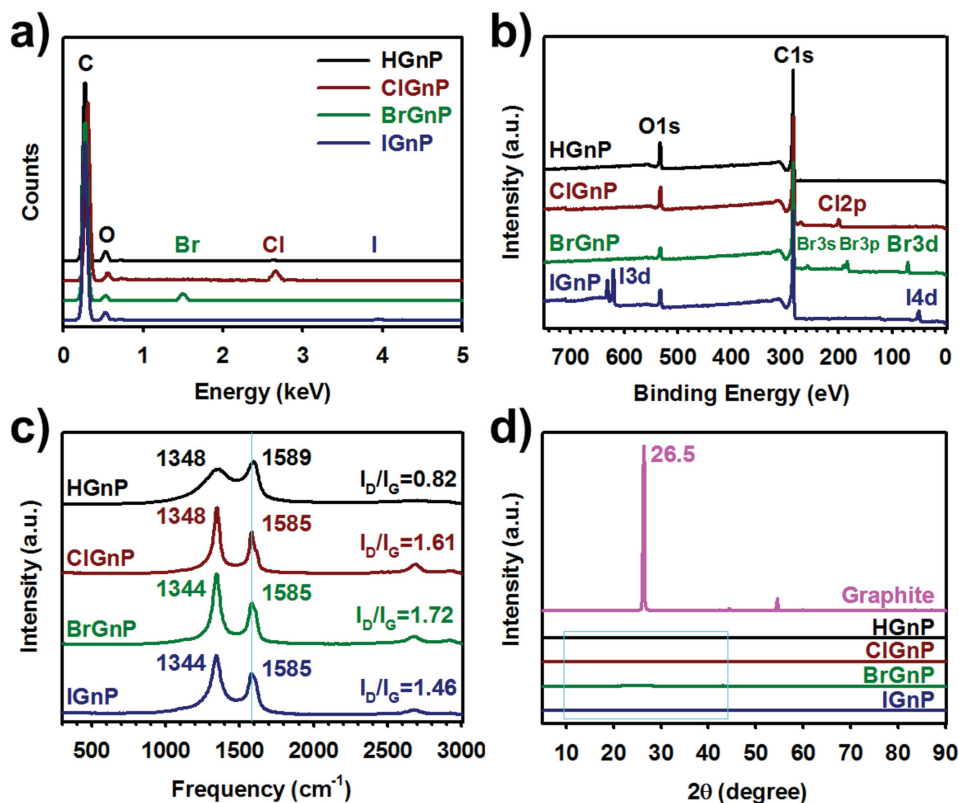


Figure 2. (a) EDX spectra (FE-SEM). Corresponding element mappings are presented in Figure S1; (b) XPS survey spectra. High-resolution XPS spectra of Cl, Br and I for ClGnP, BrGnP and IGnP, respectively, are presented in Figures S2a–S2c; (c) Raman spectra obtained with 532 nm wavelength; (d) XRD patterns. Magnified XRD patterns from the sky blue rectangle are presented in Figure S2d. The relative intensities of HGnP and XGnPs (X = Cl, Br or I) are less than 0.4% to that of the pristine graphite, indicating that ball-milled GnPs are highly exfoliated into a few layers.

a lower I_D/I_G ratio of 0.82 than those of XGnPs. In addition to the substantial size reduction for all samples to show increased D band with respect to that of the graphite starting material (not shown) due to the enhanced edge-effect, the higher I_D/I_G ratios for XGnPs with similar grain size (see Figures 1b–1e) is attributable to the much larger atomic size of halogens (atomic radii of 0.99–1.33 Å) than that of hydrogen (0.37 Å) in HGnP. Although the less ordered carbon could favor more lithium storage during the discharge/charge process, the more ordered carbon is beneficial for efficient electron transport. Thus, an optimum ratio of I_D/I_G for XGnPs could lead to enhanced electrochemical performance. The order of inherent electronic conductivities of XGnPs is $2.201 \times 10^{-4} \text{ S cm}^{-1}$ (X = I), $2.069 \times 10^{-4} \text{ S cm}^{-1}$ (X = Cl), $1.996 \times 10^{-4} \text{ S cm}^{-1}$ (X = H) and $6.713 \times 10^{-6} \text{ S cm}^{-1}$ (X = Br), indicating the highest conductivity of IGnP and the lowest conductivity of BrGnP.

Furthermore, XRD diffraction patterns in Figure 2d show that the strong sharp [002] peak at 26.5° corresponding to an interlayer d -spacing of graphite (0.34 nm) reduced to less than 0.4% for all the ball-milled samples, indicating that most graphitic layers of HGnP and XGnPs were delaminated into a few layers of GnPs. The enlarged view of the sky blue rectangle area in Figure 2d is given in Figure S6d, which shows that the main peaks of HGnP and XGnPs shifted to lower angles and became broader due to their larger interlayer distance and broader interlayer distance distribution than the pristine graphite. The

observed morphological changes will lead to enhanced kinetics for lithium-ion insertion/extraction and more lithium-ion storage (vide infra).^[10]

Compared with the pristine graphite ($2.8 \text{ m}^2 \text{ g}^{-1}$, Table S2), Brunauer-Emmett-Teller (BET) surface areas of HGnP and XGnPs (X = Cl, Br or I) were profoundly increased in the range of $439.2\text{--}736.8 \text{ m}^2 \text{ g}^{-1}$, supporting that large degree of delamination occurred by edge-functionalization during ball-milling graphite. In addition, as atomic size ($\text{H} < \text{Cl} < \text{Br} < \text{I}$) increases at the edges, the BET surface areas accordingly increases in the order of HGnP < ClGnP < BrGnP < IGnP. Thus, the dopant atomic size is one of the significant factors for the exfoliation of graphitic layers as schematically presented in Figure S7. This result is well correlated with XRD patterns of the HGnP and XGnPs compared with that of the pristine graphite (Figure 2d). On the basis of the maximum BET surface of single layer graphene ($2630 \text{ m}^2 \text{ g}^{-1}$) and negligible surface areas at the edges (Figure S8), the average number of layers could be estimated to be 6.0 (HGnP), 4.6 (ClGnP), 4.2 (BrGnP) and 3.6 (IGnP).

Having performed the structure characterization for HGnP and XGnPs (X = Cl, Br or I), the initial discharge/charge profiles of these samples at 0.1 C in the voltage range of 0.02 – 3.0 V were scanned (Figure 3a). The shape of the discharge/charge profiles are typical behaviors of carbonaceous materials.^[9] The results are in accordance with the cyclic voltammetry (CV) analysis. Figure S9 shows the initial 5 cycles cyclic voltammograms

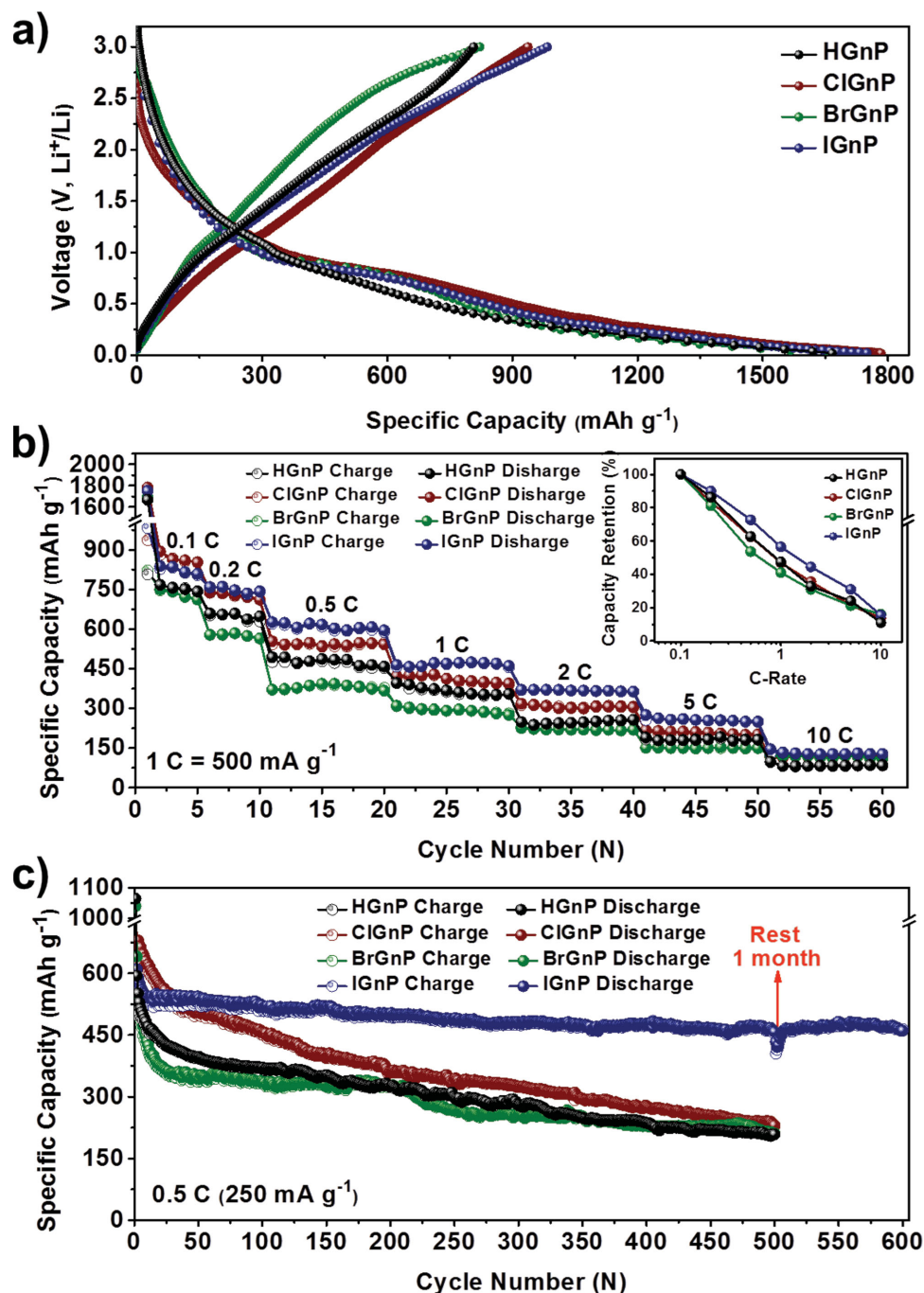


Figure 3. (a) Initial discharge-charge curves at 0.1 C; (b) rate performance. Inset charge capacity retention at various current densities; (c) cycling performance at 0.5 C of HGnP and XGnPs (X = Cl, Br or I) in the voltage range of 0.02 – 3.0 V, the continued cycling performance of the IGnP cell was obtained after 500 cycles and 1 month storage at ambient condition (25 °C).

(CV) for HGnP and XGnPs at a scan rate of 0.1 mV s⁻¹ in the voltage range of 0.02 – 3.0 V. In all cases, the first cathodic peaks centered at around 0.6 V appeared in the 1st cycle and then disappeared in the following cycles. The results indicated that a dense solid electrolyte interphase (SEI) layer was formed on the sample surfaces in the first cycle. The second cathodic peak centered at 0.05 V was ascribed to lithium-ion insertion into the graphitic layers.^[11] Besides, there are some minor peaks in

the cathodic-anodic swipes, which are most likely resulted from the residual oxygen-containing functional groups within the HGnP and XGnP samples, such as carboxylic acid and hydroxy groups (see Figure 1a). It is well known that the high irreversible capacity (low initial Coulombic efficiency) of graphene based electrode is mainly due to the reaction of lithium ion with oxygen containing functional groups in the discharge process. However, appropriate content of oxygen containing functional

groups in XGnPs (H > I > Cl > Br, Table S1) could be beneficial for the formation of strong and stable SEI on the surface area.

To compare the rate capability of HGnP and XGnPs (X = Cl, Br or I), the cells were tested for 60 cycles at current densities varying from 0.1 C to 10 C in the voltage range of 0.02 – 3.0 V. As shown in Figure 3b, the discharge capacities of HGnP, ClGnP, BrGnP and IGnP were 1666.9 (HGnP), 1783.6 (ClGnP), 1690.4 (BrGnP) and 1750.3 (IGnP) mAh g⁻¹, respectively, with charge capacities of 807.4 (HGnP), 937.6 (ClGnP), 822.1 (BrGnP) and 983.9 (IGnP) mAh g⁻¹. As expected, IGnP displayed the higher Coulombic efficiency of 56.2% compared with HGnP (48.4%), ClGnP (52.6%) and BrGnP (48.6%). Furthermore, IGnP also showed a higher rate capacity than the others at ≥0.5 C (inset of Figure 3b). As presented in Figure 3c, the relatively long-term cycling performance for samples are compared at 0.5 C in the voltage range of 0.02 – 3.0 V. It can be found that HGnP, ClGnP, BrGnP and IGnP had initial charge capacities of 511.3 (HGnP), 626.5 (ClGnP), 546.8 (BrGnP) and 562.8 (IGnP) mAh g⁻¹, respectively. After 500 cycles, the sample cells delivered the charge capacities of 208.5 (HGnP), 229.5 (ClGnP), 210.6 (BrGnP), and 458.0 mAh g⁻¹ (IGnP), with initial charge capacity retention of 40.8%, 36.6%, 38.5% and 81.4%, respectively. Once again, the IGnP showed the best cycling performance. Apart from the high surface area of IGnP (Table S2), the excellent rate capability and cycling performance of IGnP are also attributed to the high electronegativity of I ($\chi = 2.66$) that is higher than that of carbon ($\chi = 2.55$) as well as the enlarged entrance of functional edges that is due to relatively larger atomic size of iodine ($d_{\text{I}} > d_{\text{Br}} > d_{\text{Cl}} > d_{\text{H}}$) at the edges of GnPs to facilitate the insertion/extraction between graphitic layers.^[13] Moreover, it should be noted that the IGnP cell after 500 cycle measurements and 1 month storage at ambient condition (25 °C) still showed a reversible capacity of 464.1 mAh g⁻¹ at the 600th cycle. The capacity in the 501th cycle after 1 month storage was 404.9 mAh g⁻¹ and then increased in the initial cycles (arrow of Figure 3c), which is attributed to the re-activation of electrode/electrolyte. The outstanding cycling data for the IGnP further indicate that the IGnP electrode is very stable and active anode for LIBs.

Electrochemical impedance spectroscopy (EIS) was widely used to investigate electrodes kinetics.^[20] Figures 4a–4d show the Nyquist plots of the sample electrodes at the discharged state of 1.0 V (vs. Li⁺/Li) after discharge/charge for 5 cycles at different temperatures. The impedance curves of all samples show a semicircle in the medium frequency region, which could be assigned to the lithium-ion diffusion through the solid electrolyte interphase (SEI) film (R_s) and the charge transfer resistance (R_{ct}), respectively, and a clear -45° inclined line in the low-frequency region, which could be considered to be a Warburg impedance (W). The R_{ct} is calculated using the equivalent circuit shown in Figure S10, in which the equivalent circuit model also includes internal resistance (R_e , e.g., electrolyte resistance, contact resistances between particles and/or between electrode and current collector), a constant phase element (CPE-1) and a non-ideal constant phase element (CPE-2). The values of the parameter R_{ct} obtained from a nonlinear least squares fitting are summarized in Figure S11, in which IGnP had the smaller R_{ct} values at different temperatures than the other XGnPs (X = H, Cl or Br), indicating the enhancement in the kinetics and

the consequent improvement in the rate capability of IGnP. To understand the mechanism of the capacity fading after intensive cycling of XGnPs (X = H, Cl or Br), the EIS measurements for XGnPs were carried out at the discharge state of 1.0 V after different cycles at 0.5 C in the voltage range of 0.02 – 3 V (Figure S12). The corresponding fitting results were shown in Figure S13. The total impedance of XGnPs (X = H, Cl, Br or I) decreased initially, and then began to slowly increase from the 50th cycle to the 200th cycle. The enhanced reaction kinetics in the initial cycles is attributed to electrode-electrolyte activation. After 50 cycles, for the R_e , R_s and R_{ct} of XGnPs (X = H, Cl or Br) electrodes, impedances were more increased than that of IGnP electrode, indicating the large internal resistance, the unstable and thicker SEI formation and worsened kinetics for XGnPs (X = H, Cl or Br), respectively.

The apparent activation energies of samples were further investigated to understand the kinetics of the charge-transfer reaction.^[21] The exchange current (i_0) and the apparent activation energy (E_a) for the lithium intercalated into samples can be calculated from the Arrhenius Equations (1) and (2), respectively:

$$i_0 = RT/(nFR_{ct}) \quad (1)$$

$$i_0 = A \exp(-E_a/RT) \quad (2)$$

where A is a temperature-independent coefficient, R is the gas constant, T (K) is the absolute temperature, n is the number of transferred electrons, F is Faraday constant and E_a is apparent activation energy. Figure 4e shows the Arrhenius plots of $\log_{10}i_0$ as a function of 1/T. The apparent activation energies ($E_a = -Rk \ln 10$, where k = the slope of the fitting line in Figure 4e) which were calculated to be 38.7, 35.3, 39.4 and 35.1 kJ mol⁻¹ for HGnP, ClGnP, BrGnP and IGnP, respectively. These results indicate that IGnP has a lower apparent activation energy for the extraction of lithium-ions from host structures than those of HGnP and the other XGnPs (X = Cl or Br). These results agree well with the electrochemical performance shown in Figures 3b and 3c. To better compare the different electrochemical performance of XGnPs, the key parameters affecting the electrochemical performance are summarized in the Table S3. The IGnP delivered the best electrochemical performance with the highest electronic conductivity, the highest surface area, the largest edge-to-edge distance between the graphitic layers, the lowest SEI resistance and the highest charge transfer resistance, while the BrGnP with the lowest electronic conductivity, the highest SEI resistance and the highest charge transfer resistance.

In summary, the electrochemical performance of edge-selectively hydrogenated (HGnP) and halogenated GnPs (XGnPs, X = Cl, Br or I) prepared by ball-milling has been investigated as anode materials for LIBs. It has been found that the IGnP electrode can deliver an initial charge capacity of 562.8 mAh g⁻¹, at 0.5 C in the voltage range of 0.02 – 3.0 V, which is higher than the corresponding value of 511.3 mAh g⁻¹ for the HGnP counterpart. After 500 cycles, the IGnP electrode retained a higher charge capacity of 458.0 mAh g⁻¹ with initial charge capacity retention of 81.4% compared to the HGnP electrode with 208.5 mAh g⁻¹ and 40.8%. Furthermore, the IGnP cell measured

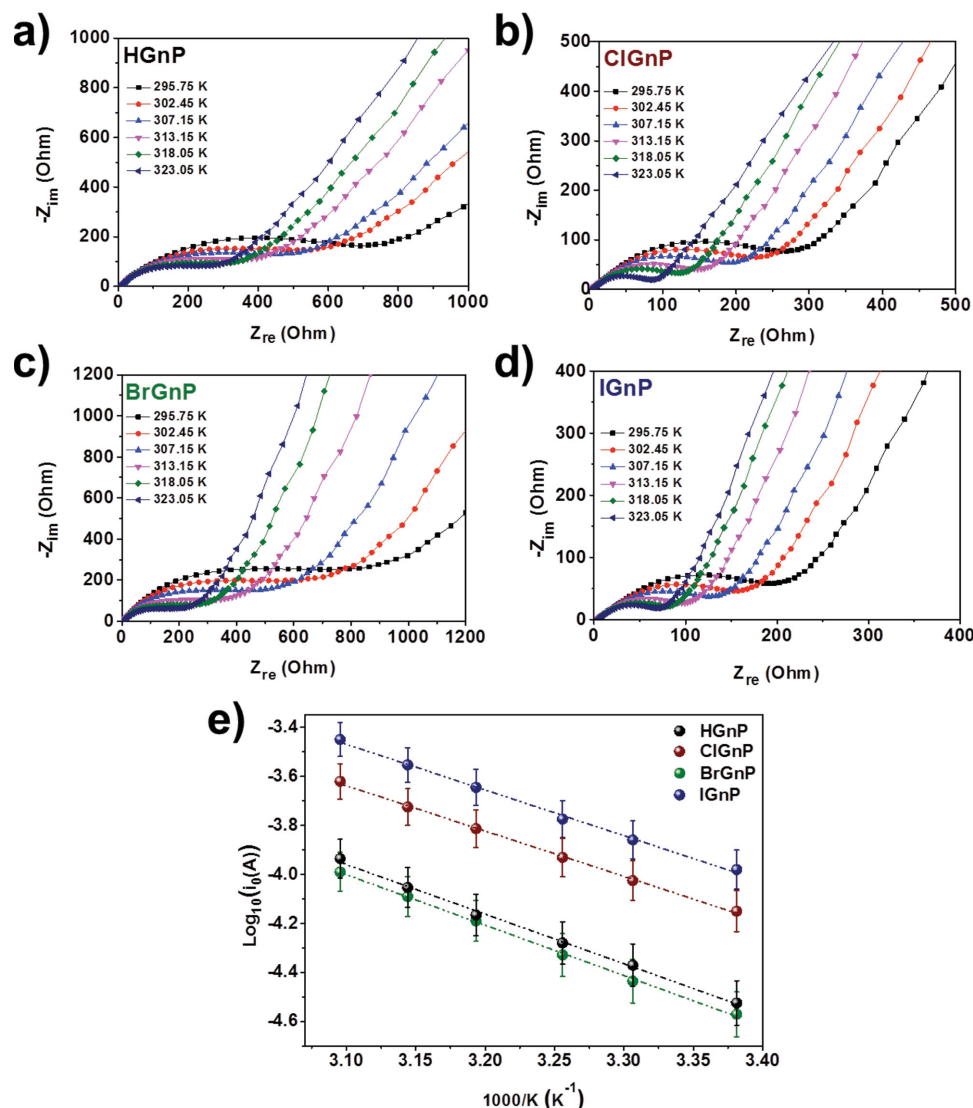


Figure 4. Nyquist plots of (a) HGnP, (b) ClGnP, (c) BrGnP, and (d) IGnP at the discharged state of 1.0 V (*vs.* Li⁺/Li) at different temperatures and at frequencies from 1 MHz to 10 mHz. The equivalent circuit is shown in Figure S10. (e) Arrhenius plots of $\log i_0$ versus $1/T$ for HGnP and XGnP (X = Cl, Br or I). The lines are the linear fitting results.

after 500 cycles and 1 month storage at ambient condition (25 °C) still maintained a reversible capacity of 464.1 mAh g⁻¹ after remeasurements for 100 cycles, indicating the highly stable nature of IGnP. These results demonstrate that IGnP prepared by the low-cost, large-scale ball-milling production is of great potential as a promising anode material for high energy LIBs.

programs through the National Research Foundation (NRF) of Korea, VPP program supported by King Saud University and AFOSR (FA9550-12-1-0037, FA-9550-12-1-0069), NSF (NSF-CMMI-1400274, NSF-AIR-II-1343270) and Auto CRC 2020. The authors acknowledge use of the facilities (Australian Research Council (ARC) – Linkage, Infrastructure, Equipment and Facilities (LIEF) grant (LE120100104)) and the assistance of Dr. Gilberto Casillas at the University of Wollongong Electron Microscopy Centre.

Supporting Information

Supporting Information is available from the Wiley Online Library or from the author.

Acknowledgements

The authors are grateful for financial support from BK21 Plus, Mid-Career Researcher (MCR) and Basic Research Laboratory (BRL)

Received: July 6, 2014
Revised: August 5, 2014
Published online: September 19, 2014

- [1] V. Etacheri, R. Marom, R. Elazari, G. Salitra, D. Aurbach, *Energ. Environ. Sci.* **2011**, *4*, 3243.
- [2] a) Y. Wang, G. Cao, *Adv. Mater.* **2008**, *20*, 2251; b) A. Kraysberg, Y. Ein-Eli, *Adv. Energy Mater.* **2012**, *2*, 922; c) J. Xu, S. Dou, H. Liu, L. Dai, *Nano Energy* **2013**, *2*, 439.
- [3] G. G. Amatucci, N. Pereira, *J. Fluorine Chem.* **2007**, *128*, 243.

- [4] a) W. R. Liu, S. H. Wu, H. S. Sheu, *J. Power Sources* **2005**, *146*, 232; b) X. L. Li, F. Y. Kang, W. C. Shen, X. D. Bai, *Electrochim. Acta* **2007**, *53*, 1761; c) J. Yan, W. Yuan, Z.-Y. Tang, H. Xie, W.-F. Mao, L. Ma, *J. Power Sources* **2012**, *209*, 251; d) J. Yan, W. Yuan, Z. Y. Tang, H. Xie, W. F. Mao, L. Ma, *J. Power Sources* **2012**, *209*, 251; e) S. X. Liu, H. L. Zhang, *Rare Metal Mat. Eng.* **2013**, *42*, 296; f) W. K. Kim, D. W. Han, W. H. Ryu, S. J. Lim, J. Y. Eom, H. S. Kwon, *J. Alloy. Compd.* **2014**, *592*, 48.
- [5] a) Z. Y. Chen, H. L. Zhu, G. R. Hu, J. Xiao, Z. D. Peng, Y. X. Liu, *T Non-ferr. Metal Soc.* **2004**, *14*, 1151; b) Y. H. Chen, Q. S. Jiao, L. Wang, Y. W. Hu, N. Sun, Y. S. Shen, Y. H. Wang, *Cr. Chim.* **2013**, *16*, 845.
- [6] J. Kim, A. Manthiram, *Nature* **1997**, *390*, 265.
- [7] a) G. Ceder, Y.-M. Chiang, D. Sadoway, M. Aydinol, Y.-I. Jang, B. Huang, *Nature* **1998**, *392*, 694; b) C. Frayret, A. Villesuzanne, N. Spaldin, E. Bousquet, J.-N. Chotard, N. Recham, J.-M. Tarascon, *Phys. Chem. Chem. Phys.* **2010**, *12*, 15512.
- [8] a) G. Du, N. Sharma, V. K. Peterson, J. A. Kimpton, D. Jia, Z. Guo, *Adv. Funct. Mater.* **2011**, *21*, 3990; b) F. Wang, R. Robert, N. A. Chernova, N. Pereira, F. Omenya, F. Badway, X. Hua, M. Ruotolo, R. Zhang, L. Wu, V. Volkov, D. Su, B. Key, M. S. Whittingham, C. P. Grey, G. G. Amatucci, Y. Zhu, J. Graetz, *J. Am. Chem. Soc.* **2011**, *133*, 18828.
- [9] E. Yoo, J. Kim, E. Hosono, H.-S. Zhou, T. Kudo, I. Honma, *Nano Lett.* **2008**, *8*, 2277.
- [10] D. Pan, S. Wang, B. Zhao, M. Wu, H. Zhang, Y. Wang, Z. Jiao, *Chem. Mater.* **2009**, *21*, 3136.
- [11] a) G. Wang, X. Shen, J. Yao, J. Park, *Carbon* **2009**, *47*, 2049; b) A. V. Murugan, T. Muraliganth, A. Manthiram, *Chem. Mater.* **2009**, *21*, 5004.
- [12] a) A. L. M. Reddy, A. Srivastava, S. R. Gowda, H. Gullapalli, M. Dubey, P. M. Ajayan, *ACS Nano* **2010**, *4*, 6337; b) Z. S. Wu, W. C. Ren, L. Xu, F. Li, H. M. Cheng, *ACS Nano* **2011**, *5*, 5463; c) C. Zhang, N. Mahmood, H. Yin, F. Liu, Y. Hou, *Adv. Mater.* **2013**, *25*, 4392.
- [13] I. Y. Jeon, H. J. Choi, M. Choi, J. M. Seo, S. M. Jung, M. J. Kim, S. Zhang, L. P. Zhang, Z. H. Xia, L. M. Dai, N. Park, J. B. Baek, *Sci. Rep.-UK* **2013**, *3*, 2260.
- [14] a) I. Y. Jeon, Y. R. Shin, G. J. Sohn, H. J. Choi, S. Y. Bae, J. Mahmood, S. M. Jung, J. M. Seo, M. J. Kim, D. W. Chang, L. M. Dai, J. B. Baek, *P. Natl. Acad. Sci. USA* **2012**, *109*, 5588; b) I. Y. Jeon, H. J. Choi, S. M. Jung, J. M. Seo, M. J. Kim, L. M. Dai, J. B. Baek, *J. Am. Chem. Soc.* **2013**, *135*, 1386.
- [15] L. Qu, Y. Liu, J.-B. Baek, L. Dai, *ACS Nano* **2010**, *3*, 1321.
- [16] K. S. Subrahmanyam, L. S. Panchakarla, A. Govindaraj, C. N. R. Rao, *J. Phys. Chem. C* **2009**, *113*, 4257.
- [17] W. S. Hummers, R. E. Offerman, *J. Am. Chem. Soc.* **1958**, *80*, 1339.
- [18] a) S.-M. Jung, E.-K. Lee, D. Shin, I.-Y. Jeon, J.-M. Seo, H.-Y. Jeong, N. Park, J.-H. Oh, J.-B. Baek, *Angew. Chem. Int'l Ed.* **2014**, *53*, 2398–2401; b) Y. Zhu, S. Murali, W. Cai, X. Li, J. W. Suk, J. R. Potts, R. S. Ruoff, *Adv. Mater.* **2010**, *22*, 3906; c) Y. Sun, Q. Wu, G. Shi, *Energ. Environ. Sci.* **2011**, *4*, 1113; d) L. Dai, *Acc. Chem. Res.* **2012**, *46*, 31.
- [19] I.-Y. Jeon, H.-J. Choi, S.-M. Jung, J.-M. Seo, M.-J. Kim, L. Dai, J.-B. Baek, *J. Am. Chem. Soc.* **2012**, *135*, 1386.
- [20] D. Aurbach, B. Markovsky, I. Weissman, E. Levi, Y. Ein-Eli, *Electrochim. Acta* **1999**, *45*, 67.
- [21] Y. Yamada, Y. Iriyama, T. Abe, Z. Ogumi, *J. Electrochem. Soc.* **2010**, *157*, A26.